

Narrow-band single-photon emission through selective aryl functionalization of zigzag carbon nanotubes

Avishek Saha^{1,7}, Brendan J. Gifford^{1,2,3,7}, Xiaowei He¹, Geyou Ao⁴, Ming Zheng⁴, Hiromichi Kataura⁵, Han Htoon¹, Svetlana Kilina³, Sergei Tretiak^{1,3,6*} and Stephen K. Doorn^{1*}

The introduction of sp^3 defects into single-walled carbon nanotubes through covalent functionalization can generate new light-emitting states and thus dramatically expand their optical functionality. This may open up routes to enhanced imaging, photon upconversion, and room-temperature single-photon emission at telecom wavelengths. However, a significant challenge in harnessing this potential is that the nominally simple reaction chemistry of nanotube functionalization introduces a broad diversity of emitting states. Precisely defining a narrow band of emission energies necessitates constraining these states, which requires extreme selectivity in molecular binding configuration on the nanotube surface. We show here that such selectivity can be obtained through aryl functionalization of so-called 'zigzag' nanotube structures to achieve a threefold narrowing in emission bandwidth. Accompanying density functional theory modelling reveals that, because of the associated structural symmetry, the defect states become degenerate, thus limiting emission energies to a single narrow band. We show that this behaviour can only result from a predominant selectivity for *ortho* binding configurations of the aryl groups on the nanotube lattice.

Obtaining a uniformity of response in nanoscale light emitters is essential for them to be effective in applications as sensing and imaging agents and as photon sources in light-emitting diodes (LEDs), lasers and so on. In the context of emerging roles for low-dimensional nanoemitters (including colloidal and epitaxial quantum dots^{1,2}, 2D transition metal dichalcogenides^{3–6}, hexagonal boron nitride⁷ and single-walled carbon nanotubes (SWCNTs)^{8–12}) as single-photon sources for quantum metrology and quantum information processing¹³, even tighter limits on the allowed variability in emission energies are required, ultimately with the goal of achieving photon indistinguishability. Among these diverse material platforms for quantum emission, SWCNTs offer several advantages originating from the ability to control light emission properties through chemical manipulation. SWCNT emission energies are broadly tunable due to their strong dependence on the specific nanotube structure (designated by chiral indices (n,m) , Fig. 1)¹⁴. Chemical control over the surface structure of non-covalently bound wrapping agents (such as surfactants, polymers and DNA) has provided highly effective routes to isolating specific SWCNT structures in high yield and at high levels of purity, providing remarkable selectivity over emission properties¹⁵. Such surface chemistry also provides a route to control the surrounding environment for optimization of photoluminescence. Recent expansion of SWCNT emission behaviours through the introduction of photoluminescent defect states by low-level covalent functionalization provides additional synthetic tunability in emission properties and imparts quantum emission function, but also acts as a source of spectral diversity.

Functionalization of SWCNTs with ether or epoxide^{16,17}, alkyl¹⁸ and aryl¹⁹ species generates defect states whose near-infrared photoluminescence appears redshifted (by 100–300 meV) from normal SWCNT band-edge E_{11} exciton emission. Exciton localization at the defect sites boosts photoluminescence quantum yields^{16,19,20} and introduces new SWCNT functionality, including enhanced photoluminescence imaging¹⁶, photon upconversion²¹ and room-temperature single-photon emission^{11,12}. Independent of the chemistry used to introduce the defect states, photoluminescence appears over a broad (~140 meV) energy range^{12,17,22–24}. This spectral diversity effectively arises due to the potential for generation of multiple distinct chemical species as a result of the functionalization approaches^{17,22}. Of particular interest is aryl functionalization using diazonium reagents, which can provide a high degree of synthetic tunability of the defect states¹⁹ and introduces superior single-photon emission behaviours¹². Despite the relative simplicity of the diazonium chemistry, aryl attachment is accompanied by complex spectral behaviour^{12,22,23}. This complexity originates in the fact that binding of an aryl group at one SWCNT carbon site leads to an intermediate in which a reactive unpaired electron exists at an adjacent carbon (*ortho* position) or three carbons away (*para* position), thus creating six different possible binding configurations (Fig. 1b). An –H or –OH group subsequently attaches at this reactive site. Because of the chiral structure of the SWCNT, each of these six binding configurations represents a different chemical species with similar binding energies, each with its own electronic structure and emission energy^{22,25}. While the resultant spectroscopic diversity allows one to access a broad range of emission wavelengths with a

¹Center for Integrated Nanotechnologies, Materials Physics and Applications Division, Los Alamos National Laboratory, Los Alamos, NM, USA. ²Center for Nonlinear Studies, Los Alamos National Laboratory, Los Alamos, NM, USA. ³Department of Chemistry and Biochemistry, North Dakota State University, Fargo, ND, USA. ⁴Materials Science and Engineering Division, National Institute of Standards and Technology, Gaithersburg, MD, USA. ⁵Nanomaterials Research Institute, National Institute of Advanced Industrial Science and Technology (AIST), Tsukuba, Ibaraki, Japan. ⁶Theoretical Division, Los Alamos National Laboratory, Los Alamos, NM, USA. ⁷These authors contributed equally to this work: Avishek Saha, Brendan J. Gifford.

*e-mail: serg@lanl.gov; skdoorn@lanl.gov

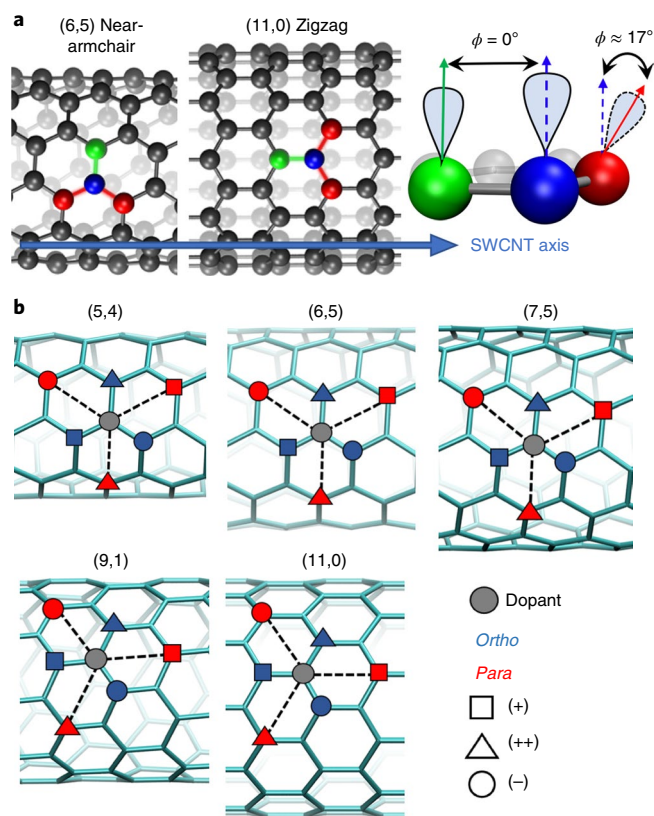


Fig. 1 | Chirality dependence of aryl diazonium binding configurations. a, Comparison of (6,5) near-armchair and (11,0) zigzag structures showing the change in bond orientations relative to the SWCNT axis. Bonds highlighted in red (on both chiral structures) are those expected to be more reactive based on having a large π -orbital misalignment angle (ϕ of $\sim 17^\circ$, ref. ²⁷, illustrated on the right) between the aryl binding site (blue sphere) and the carbon atom at which the unpaired electron resides (red spheres). Bonds highlighted in green (on both chiral structures) have ϕ of $\sim 0^\circ$ and are expected to be most stable. **b**, Illustration of the six different available binding configurations relative to the aryl binding site (grey circle) for five SWCNT chiralities. Configurations are defined by the carbon site at which the unpaired electron—resulting from aryl binding—captures a -H or -OH group and may be located one (*ortho*, blue) or three (*para*, red) carbons away. SWCNT chiral structure dictates that each of the six configurations is chemically distinct for all non-zigzag structures, further distinguished by the +, ++ and - labels (square, triangle and circle symbols, respectively). For the (11,0) zigzag structure, the *ortho* (++, -) configurations are identical by symmetry, as are the *para* (++, -) configurations. Although resonance structures may exist for which the unpaired electron is located more than three carbons from the aryl site, such configurations produce non-emissive states^{22,25,49}.

single nanotube chirality (providing a versatile route to access the telecom region, 1,300–1,500 nm)¹², such a broad emission response from tube to tube in any given sample will limit their utility for applications. Therefore, devising a strategy for providing selectivity in the binding chemistry is highly desired.

Aryl diazonium chemistry has been demonstrated to show selectivity for metallic SWCNTs in comparison to reactivity with semi-conducting types and is driven primarily by a difference in redox behaviour between the two electronic types²⁶. Such type selectivity, however, is inadequate in terms of the goal of configurational selectivity of binding only to a single predetermined site. Nanotube reactivity is dependent on both the π -orbital pyramidalization

angle (related to sidewall curvature, and thus nanotube diameter) and π -orbital misalignment angle between participating reactive sites²⁷. The latter is dependent on whether respective bonds are oriented along or perpendicular to the nanotube axis (Fig. 1a), will be highly dependent on nanotube chirality, and is thus likely to be most closely linked to the goal of configurational selectivity. So far, such orientational control over reactivity has not yet been demonstrated. Constraining defect-state spectral response, however, requires exactly that degree of control. The configurational picture illustrated in Fig. 1 suggests that ultimate control over binding may be obtained by controlling the interplay between nanotube structure, structure of the molecular dopant, and the surface structures formed on coating the nanotube with suspension agents. Although a rich functionalization chemistry is available for graphene and carbon nanotubes^{27–29}, the precise chemistry of binding is not yet understood at an atomistic and single-bond level, the level of understanding and control required to chemically constrain defect-state emission energies. Here, we probe defect-state spectral evolution as a function of SWCNT chirality and surface coating. In the limit of pure zigzag structures (chiral indices $(n,0)$), the photoluminescence spectrum collapses to a single narrow, highly redshifted emission band. Quantum chemical modelling of zigzag SWCNT electronic structure provides an atomistic understanding of the aryl binding and indicates that such narrowing of the response is due to binding sites becoming degenerate due to the SWCNT symmetry. Moreover, this result is strongly suggestive that only *ortho* binding configurations are selected following aryl functionalization.

Results and discussion

Defect-state spectral dependence on SWCNT chiral angle. To assess the potential role of nanotube structure in defining configurational binding and in constraining defect-state emission wavelengths, we obtained photoluminescence spectra that were highly enriched in respective single SWCNT chiralities (see Methods) for structures varying in chiral angle (θ) from the near-armchair ($n=m$) (6,5) structure ($\theta=27^\circ$) to (7,5) ($\theta=24.5^\circ$) and near zig-zag (10,3) structures ($\theta=12.73^\circ$). The chiral angle defines the direction at which a graphene sheet may be rolled up to form a specific SWCNT structure and also determines the degree to which C–C bonds in the SWCNT structure are offset from the parallel or perpendicular directions with respect to the SWCNT axis¹⁴. As shown in Fig. 2a–c, defect-state emission features in the probed nanotubes appear as two emission bands for SWCNTs functionalized with 4-methoxybenzene, labelled E_{11}^+ (shifted by about 100 meV to lower energy from the band-edge E_{11} exciton) and the lower-energy E_{11}^{*-} band (redshifted by ~ 150 – 200 meV). Importantly, as one progresses to smaller chiral angles, the E_{11}^+ band grows in intensity relative to the E_{11}^{*-} band, which is suggestive of chiral angle-dependent selectivity over the emission band.

It should be noted that, across this chirality series, the nanotube diameter also increases (from 0.76 nm for (6,5) to 0.94 nm for (10,3)), and the changing diameter must also be considered as a potential factor in determining the observed spectral features. We therefore also obtained photoluminescence spectra for 4-methoxybenzene-functionalized (9,1)-enriched SWCNTs. The (9,1) structure has an identical diameter as the (6,5), but, being a near-zigzag structure, has a much smaller chiral angle ($\theta=5.21^\circ$). As seen in Fig. 2d, the (9,1) photoluminescence spectrum continues the chiral angle-dependent trend of increasing intensity in the E_{11}^+ band, which now dominates the spectrum. This result eliminates diameter as the determining factor in the spectral changes. Carrying the chiral angle dependence one step further, we also probed the photoluminescence response of the (11,0) true zigzag structure ($\theta=0^\circ$) and found that the defect-state emission now consists nearly exclusively of the E_{11}^{*-} band (1,326 nm (0.935 eV), Fig. 2e), which is accompanied by additional weak

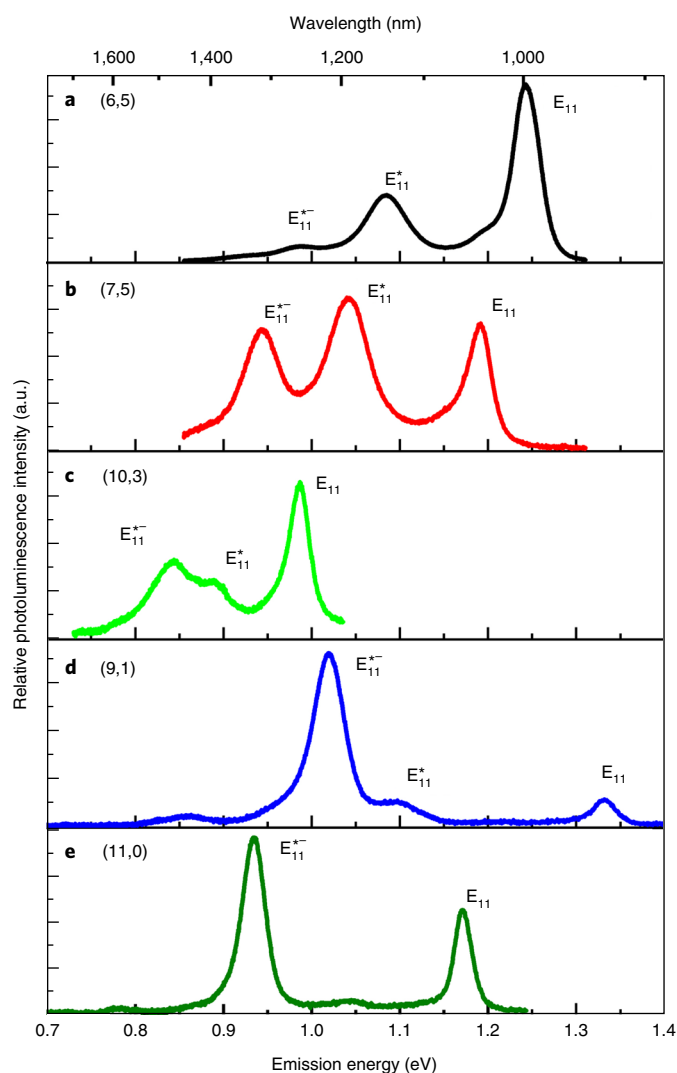


Fig. 2 | Chirality dependence of defect-state photoluminescence spectra.

a–e, Photoluminescence spectra (obtained with excitation at or near the E_{22} transition) of different SWCNT chiralities functionalized with 4-methoxybenzene in a 1% sodium dodecyl sulfate environment, with each sample highly enriched in the respective single chirality (see Methods): (6,5), black trace, excitation at 570 nm (**a**); (7,5), red trace, excitation at 650 nm (**b**); (10,3), light green trace, excitation at 635 nm (**c**); (9,1), blue trace, excitation at 700 nm (**d**); (11,0), dark green trace, excitation at 750 nm (**e**). All spectra were obtained in D_2O . Band-edge exciton (E_{11}) and defect-state (E_{11}^+ and E_{11}^-) emission bands are labelled. Note that the difference in defect-state photoluminescence intensities relative to that of E_{11} across the chirality range reflects a difference in defect concentration only. Progression in structures from nearly armchair in the case of (6,5) to the zigzag (11,0) system results in an increase in relative intensity of E_{11}^- . Spectra collapse to a single emission feature at E_{11}^+ in the zigzag limit.

photoluminescence features at 1,190 nm and 1,599 nm (1.042 and 0.775 eV, respectively).

In comparison to the photoluminescence spectrum of unfunctionalized (11,0) SWCNTs (Supplementary Fig. 1), the feature at 1,599 nm (0.775 eV) is found to result from functionalization and thus is probably also due to defect-state emission. The 1,190 nm (1.042 eV) peak overlaps with the SWCNT phonon sideband emission³⁰, but its appearance in single-tube spectra in the absence of a clear E_{11} peak (Fig. 3) indicates it also is probably

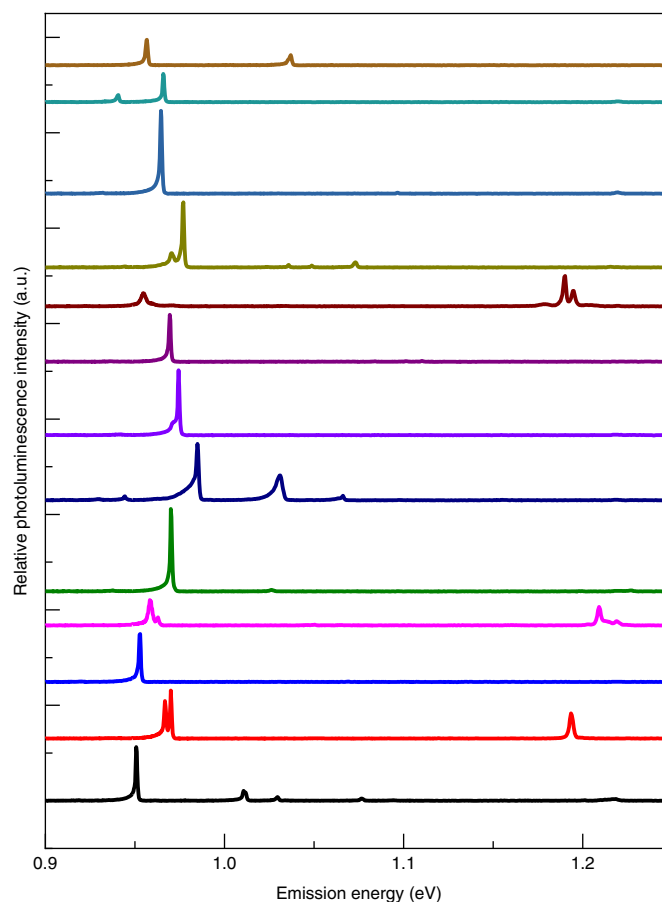


Fig. 3 | Single-tube photoluminescence spectra of 13 aryl-functionalized (11,0) nanotubes. Photoluminescence spectra obtained at 4 K of individual (11,0) SWCNTs functionalized with 4-methoxybenzene. The sample is deposited from a solution of SWCNTs that is highly enriched in the (11,0) structure. Appearance of peaks in the phonon sideband range (1.0–1.08 eV) in the absence of an E_{11} feature indicates that these particular features are due to defect-state emission. The data indicate that the limited spectral range observed at the ensemble level (Fig. 2e) extends to behaviour observed for single nanotubes at 4 K, for which defect-state emission peaks are found within a 25 meV region. More extensive statistics obtained from individual single (11,0) SWCNTs are included in Supplementary Fig. 2.

due to weak defect-state emission. The extreme narrowing of the photoluminescence emission range to that of the E_{11}^+ peak at the ensemble level, however, is reflected in the single tube spectra, which show an improved uniformity for the zigzag structures, which is of importance for single-photon emission requirements. Representative spectra for 13 individual (11,0) nanotubes functionalized with 4-methoxybenzene are shown in Fig. 3. Defect-state peaks are found primarily in the range of 0.95–0.975 eV, a span of only 25 meV. The (11,0) single-tube behaviour is in stark contrast to that previously reported for the (6,5), (7,5) and (10,3) structures, which span energy ranges of ~120–140 meV ((6,5), 0.95–1.09 eV; (7,5), 0.93–1.05 eV; (10,3), 0.785–0.905 eV)^{12,22}. The combined ensemble and single-tube spectra thus demonstrate that, as one samples chiral structures from the armchair to zigzag limits, defect-state emission is progressively moved to the more redshifted E_{11}^- band, ultimately collapsing to emission from a single state in the true zigzag limit. Towards further control over defect-state emission energies, it is important to understand the origins of this limiting behaviour.

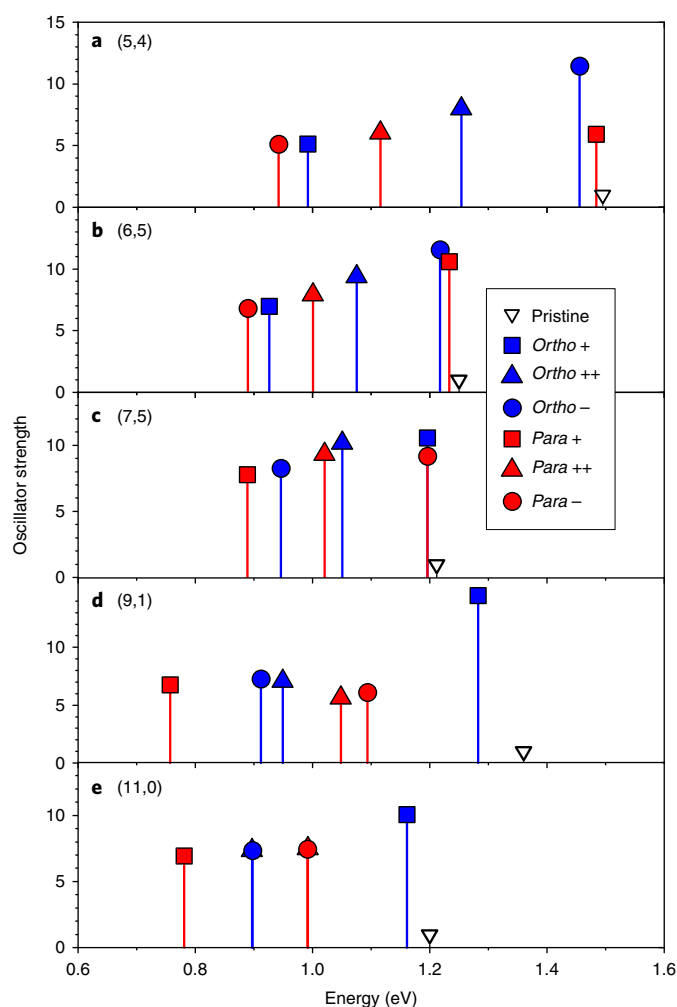


Fig. 4 | Calculated defect-state photoluminescence spectra. a–e, Chirality-dependent photoluminescence spectra determined by TD-DFT, shown for each of the possible aryl binding configurations illustrated in Fig. 1 (with identical labelling) for (5,4) (**a**), (6,5) (**b**), (7,5) (**c**), (9,1) (**d**) and (11,0) (**e**) chiralities. Expected emission energies for each defect state are shown relative to E_{11} emission (open inverted black triangle) for each chirality, with relative oscillator strengths illustrated by stick height. Note that the energy positions of the *ortho*⁺ and *ortho*⁻, and *para*⁺ and *para*⁻, features are swapped for $[(n-m) \bmod 3] = 1$ structures ((5,4) and (6,5)) in comparison to the $[(n-m) \bmod 3] = 2$ structures ((7,5), (9,1) and (11,0)), highlighting the sensitivity of the TD-DFT results to SWCNT mod value, as well as the chirality. The *ortho* (and *para*) ++ and - features become degenerate for (11,0) due to structural symmetry making the two associated binding configurations chemically identical in the zigzag limit (Fig. 1b). See also Supplementary Table 1 for mod-dependent energy trends.

Role of surface structure. Ordered surface structures arising from specific interactions between the carbon nanotube and surface wrapping agents have the potential to promote functionalization at specific carbon sites. Selectivity may be possible through masking of certain binding configurations or through the generation of steric barriers. A comparison of the photoluminescence emission spectra for different wrapping conditions may reveal such behaviours. As test systems, we chose to perform SWCNT functionalization for nanotubes suspended using sodium dodecyl sulfate (SDS) for comparison with a suspension with DNA. SDS is known to generate random disordered structures on the nanotube surface^{31–33}. In contrast, through specific interactions, DNA can generate more ordered and

even periodic surface structures^{15,34,35}. Importantly, all of the results shown in Fig. 2 are for SWCNTs initially suspended and functionalized in SDS, which is not expected to be capable of inducing binding site selectivity due to its random surface structure. Perhaps more unexpected is that we find the photoluminescence spectra obtained for functionalized DNA-wrapped SWCNTs are nearly identical to those found for the SDS suspensions (Supplementary Fig. 3). This is the case for all five studied chiralities. The similarity in findings between the SDS and DNA results indicates that, for the chosen system, the DNA wrapping is probably not selectively masking specific binding configurations and is not enhancing steric interactions that might drive selectivity. The lack of evidence of steric selectivity for the 4-methoxybenzene dopant may simply be a consequence of its simple structure. Reported spectra showing varying degrees of enhancement of the E_{11}^+ versus E_{11}^- for other types of dopant with more complex structures suggest that steric interactions (with surface agents or the nanotube structure itself) may still be important as a selection factor^{23,24,36}. The DNA/SDS comparison, however, demonstrates it is not likely to be the source of our observations. To better understand the spectra of Fig. 2, we turn to quantum chemical modelling of electronic structure trends as the SWCNT chiral angle is changed.

Chirality dependence of electronic structure and quantum chemical modelling. To obtain further insight into the chiral angle dependence of defect-state emission properties, we performed calculations of the relative thermodynamic stability and excited-state structure for the different possible binding configurations using density functional theory (DFT) and time-dependent DFT (TD-DFT), respectively (see Methods)^{17,22,25}. These properties were determined for several SWCNT structures (three near-armchair and two zigzag: (5,4), (6,5), (7,5), (9,1) and (11,0)). The specific configurations for each chirality are defined in Fig. 1b. Our calculated binding stabilities (Supplementary Fig. 4) indicate only the stability of the final product. No information is provided pertaining to the reactivity of particular bonds leading to each specific configuration, and thus the relative stabilities do not reflect the kinetics of the functionalization process. As such, they can only indicate if a significant thermodynamic preference for a particular configuration exists (see Methods). As an example, ether-d defect sites dominate the solution-phase ensemble photoluminescence spectrum of oxygen-functionalized SWCNTs because it is more thermodynamically stable (by 1.5 eV) compared to epoxide-1 functionality¹⁷. We find that the binding stability also differs for each of the possible aryl binding configurations represented in Fig. 1 (Supplementary Fig. 4). Relative stabilities for the near-armchair (5,4), (6,5) and (7,5) species show more variability than for the (9,1) and (11,0) zigzag structures. All calculated stabilities are within 0.6 eV of each other. Considering, however, that around 0.4 eV of this energy may be due to differences in rotational orientation of the aryl group in each binding configuration²⁵, the relative binding energies may be determined by steric effects. Therefore, the differences in these relative stabilities provide no compelling basis for significant thermodynamic selectivity of a specific configuration for the aryl defect states.

Excited-state electronic structure calculations allow the determination of the lowest-energy emissive states for each defect site configuration, to yield the model photoluminescence spectra shown in Fig. 4. Importantly, oscillator strengths for each state are found to be similar, indicating that the relative intensities of the E_{11}^+ and E_{11}^- bands in the experimental spectra directly reflect the degree to which each binding configuration is formed, with the latter being determined primarily by the reactivity of the relevant bonds (Fig. 1a). Furthermore, the calculations reveal important differences in the origins of the near-armchair versus zigzag photoluminescence behaviours. In the case of the (5,4), (6,5) and (7,5) structures, each *ortho* feature is approximately paired with a corresponding *para*

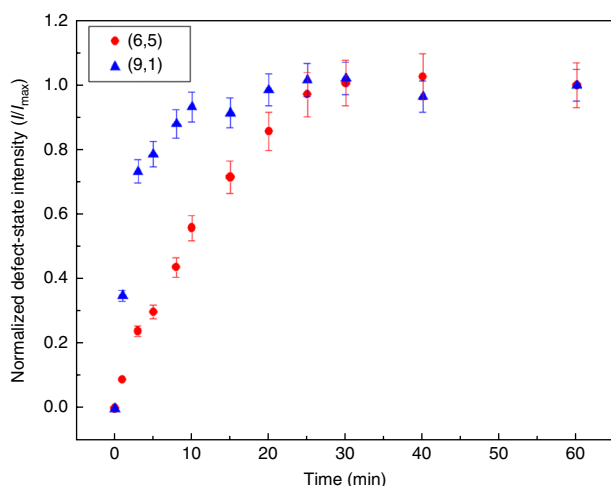


Fig. 5 | Chirality-dependent aryl-diazonium reaction kinetics. Plot of defect-state photoluminescence intensity I normalized to maximum defect-state photoluminescence intensity I_{\max} obtained on completion of the reaction, as a function of reaction time (see Methods) after introduction of 4-methoxybenzene diazonium to SWCNT solutions, for the E_{11}^* band of the (6,5) (red points) structure in comparison to the E_{11}^* band of the (9,1) (blue points) structure. SWCNT and 4-methoxybenzene diazonium reactant concentrations are identical for each experimental run (SWCNT concentrations adjusted using published absorption cross-sections as a reference point)⁴⁴. Reactions were performed at room temperature and with identical concentration of SWCNTs ($0.09 \mu\text{g ml}^{-1}$) and 4-methoxybenzene diazonium ($0.625 \mu\text{g ml}^{-1}$). The (6,5) E_{11}^* intensity rise is slower than that of (9,1), indicating faster reaction kinetics for (9,1) due to functionalization at a more reactive binding configuration than for (6,5).

feature. For the mod 1 (that is, $[(n-m) \bmod 3] = 1$) (5,4) and (6,5) chiralities, such pairing suggests that the E_{11}^* emission band observed in the experiment may correspond to a mix of emission from the *ortho*⁺⁺ and *para*⁺⁺ configurations (that is, $E_{11}^* \sim (\textit{ortho}^{++}, \textit{para}^{++})$), while $E_{11}^* \sim (\textit{ortho}^+, \textit{para}^-)$. For the mod 2 (that is, $[(n-m) \bmod 3] = 2$) (7,5), the pairing is $E_{11}^* \sim (\textit{ortho}^-, \textit{para}^+)$ (Fig. 4). Given these assignments, good correlation is found between the experimentally observed emission wavelengths and those anticipated from the TD-DFT results. In the case of the (9,1) and (11,0) zigzag structures, a significant change in energy ordering of the *ortho* and *para* configurations occurs. In the region of the defect-state emission bands, the *para*⁺⁺ and *para*⁻ configurations group together energetically, as do the *ortho*⁺⁺ and *ortho*⁻. Most dramatically, because of the symmetry of the (11,0) pure zigzag structure, the *ortho*⁺⁺ and *ortho*⁻ and the *para*⁺⁺ and *para*⁻ configurations become spatially equivalent for this structure (Fig. 1b). As a result, the associated defect states become degenerate, with a corresponding equivalence in emission energy (Fig. 4e).

The TD-DFT results for the zigzag structures are in excellent agreement with the experimental photoluminescence spectra. The closely spaced emission bands of the (9,1) SWCNT also agree well with experiment (Fig. 2d). Importantly, TD-DFT provides an explanation for the collapse of the defect-state emission spectrum to a single E_{11}^* emission feature for (11,0) (Figs. 2e and 4). Comparison of the zigzag and near-armchair results indicates that interpretation of the origin of two emission bands in the latter must be modified on one important point. The strong suppression of the E_{11}^* band for (11,0) SWCNTs indicates that formation of the *para* binding configurations is strongly inhibited and that the *ortho* configurations must be the dominant contribution to the emission spectrum. Assuming suppression of *para* defects for all chiralities, the assignment is $E_{11}^* \sim \textit{ortho}^{++}$

and $E_{11}^* \sim \textit{ortho}^+$ for mod 1 near-armchair structures ((5,4) and (6,5)). For the mod 2 (7,5) structure, $E_{11}^* \sim \textit{ortho}^{++}$ and $E_{11}^* \sim \textit{ortho}^-$ (Fig. 4). These assignments provide excellent agreement between the experimental and computational emission spectra of (6,5) and (7,5) SWCNTs. We note for all chiralities that a third *ortho* configuration is expected to emit near the E_{11} emission energy and will thus be difficult to distinguish from the band-edge exciton emission²². Similarly, a third *para* configuration is expected to emit at large redshifts for the near-zigzag and zigzag structures (Fig. 4). Such a feature is observed only weakly in the (9,1) and (11,0) emission spectra (appearing at 1,446 nm (0.858 eV) and 1,599 nm (0.775 eV), respectively; Fig. 2d,e), further supporting the conclusion that *para* configurations are minimized for the aryl diazonium reaction chemistry.

Chirality dependence of functionalization kinetics. The conclusion that the aryl defect binding occurs almost solely in the *ortho* configurations presents a specific expectation on how reaction kinetics compare between the near-armchair and zigzag structures. The *ortho*-only conclusion allows the use of the DFT results (Fig. 4) to make specific assignments of the photoluminescence bands to particular binding configurations, with each having a different associated reactivity. A determining factor in SWCNT reactivity is the π -orbital misalignment angle between carbon atoms. A higher degree of misalignment will result in a more reactive bond due to increased strain²⁷. For near-armchair structures, bonds aligned more nearly perpendicular to the SWCNT axis will have a misalignment angle near zero (less reactive), while those oriented away from such a circumferential direction will have greater misalignment angles (more reactive), as illustrated in Fig. 1a. For zigzag structures, π -orbital misalignment instead is minimized for bonds oriented along the SWCNT axis. Conversely, bonds oriented away from the axis will be more reactive (Fig. 1a). We note, however, that a second source of strain-induced reactivity is SWCNT curvature. To avoid the effect of curvature, we explore chirality-dependent differences in reactivity between near-armchair and near-zigzag structures by comparing aryl diazonium reaction kinetics for the (9,1) and (6,5) structures. Because these chiralities have identical diameter, curvature is eliminated as a potential source of difference in reactivity.

Figure 5 compares the reactivity for these contrasting structures by plotting the growth of their defect-state emission intensity with time after introduction of 4-methoxybenzene to the respective SWCNT solutions. The reaction kinetics are seen to be faster for the (9,1) structure. This result is understood as follows. Our TD-DFT results indicate that the (6,5) E_{11}^* emission band (tracked in the experiment) is due to the *ortho*⁺⁺ configuration, which is aligned along the circumference and therefore is expected to be less reactive with slower kinetics. In contrast, both the $E_{11}^* \sim \textit{ortho}^{++}$ and $E_{11}^* \sim \textit{ortho}^-$ bands observed for (9,1) originate in configurations aligned away from the nanotube axis, which should have greater strain, and thus faster reaction kinetics. This excellent agreement between the kinetics experiment and expectations established by an *ortho*-only binding picture provides additional strong support for our conclusion that primarily *ortho* configurations are formed as a result of the aryl attachment. Finally, we note that the expectations for relative bond reactivity (Fig. 1a), paired with the DFT results of Fig. 4, provide a qualitative basis for understanding the observed trend in Fig. 2, in which the defect-state E_{11}^* band increases in intensity relative to the E_{11}^* band as structures move from the armchair to zigzag limit. Across this structural series, the binding configurations leading to the formation of the E_{11}^* band progressively rotate relative to the SWCNT axis, such that they become more reactive and are therefore more preferentially formed.

Conclusions

By characterizing the defect-state photoluminescence spectra of a series of aryl-functionalized SWCNT chiralities ranging from

near-armchair to zigzag structures, we have established that emission is progressively weighted towards lower energies, such that in the zigzag limit, emission is constrained to a single highly redshifted band (E_{11}^+). Such narrowing of the spectral diversity observed in a number of previous works is an important step towards harnessing the defect states for photonics applications. Notably, the (11,0) structure is also found to act as a single-photon emitter at room temperature (Supplementary Fig. 5), adding to the range of SWCNT structures showing this behaviour^{11,12}. Furthermore, our TD-DFT modelling indicates that zigzag functionalization provides an effective route to eliminating the corresponding configurational diversity in the binding chemistry. Ultimately, our spectroscopic, theory and kinetics results all yield a self-consistent picture pointing towards aryl diazonium chemistry producing *ortho*-only binding configurations. This is a significant finding for mechanistic understanding of SWCNT chemistry, which has not previously established a case for such binding selectivity. While the resonance structures required for formation of *para* configurations are feasible, the initial carbon site bearing the reactive unpaired electron is formed at the *ortho* positions. Our results suggest that the aqueous environment of these structures promotes rapid hydrogen or hydroxyl binding at the *ortho* sites, and that formation of the *para* configurations is possibly kinetically inhibited. Towards further development of chemical control and tuning of defect-state spectral response, these results also solidify our ability to confidently assign spectral features to specific chemical defect species. Although these results establish the role of chirality in controlling defect-state spectral response, steric interactions as mediated by surface structure probably also remain important factors. Probing steric contributions to binding selectivity will probably involve the incorporation of dopants with more complex molecular structures or engineered interactions to induce stronger selective pressure with these parameters, and will be the subject of continued study.

Methods

SWCNT chirality enrichment and surfactant exchange. All spectra in this study were obtained from samples that were highly enriched in a single SWCNT chirality. (6,5) and (7,5) chirality-enriched SWCNTs suspended in 1 wt% sodium deoxycholate (DOC) were obtained following an aqueous two-phase (ATP) separation method, as described previously²⁷. Surfactant-based suspensions of enriched (10,3) material were generated using a column chromatography method as described elsewhere^{12,38}. DNA-wrapped SWCNT samples enriched in the (6,5), (7,5), (10,3), (9,1) and (11,0) chiralities were also generated using a DNA-based ATP approach, following published procedures³⁹. Before diazonium functionalization, SWCNTs generated in a 1 wt% aqueous DOC environment were exchanged into 1 wt% aqueous SDS by centrifugal filtration at 2,000 r.p.m. (730 g) in a bench-top centrifuge (Clay Adams Dynac Centrifuge, Model 0101). Typically ~250 μ l of SWCNTs suspended in 1 wt% DOC were diluted to 2–3 ml with 1 wt% SDS, followed by centrifugation in cellulose membrane-based Amicon Ultra (100K) 15 ml centrifugal filters until the volume reduced back to 250 μ l. This process was repeated once more to complete the DOC-to-SDS exchange. DNA-wrapped chirality-enriched SWCNTs were functionalized as-produced or after exchanging them into an SDS environment. In the latter case, DNA-wrapped SWCNTs were first exchanged with 0.1 wt% DOC/H₂O using membrane centrifugation, with a notable blueshift in its E_{11} absorption spectrum indicating successful exchange⁴⁰. Another centrifugation exchange was then performed with 1 wt% aqueous SDS before diazonium functionalization, as described above. For (10,3) samples, these processes were performed in D₂O instead of aqueous solution.

SWCNT functionalization. For functionalization of both SDS and DNA suspensions of (6,5), (7,5), (9,1) and (11,0) SWCNTs, initial SWCNT concentrations were adjusted so that E_{11} optical densities were in the range of 0.05–0.1 in a cuvette with 3 mm path length. Then, 2–5 μ l of 0.1–0.2 mg ml⁻¹ aqueous solution of 4-methoxybenzene diazonium tetrafluoroborate salt (Aldrich) were added to 200 μ l of SWCNTs. The doping reaction was carried out under incidental E_{22} illumination of SWCNTs while their photoluminescence spectrum was monitored to evaluate the extent of the functionalization reaction. Once a desired level of defect-state emission intensity was achieved, the reaction was quenched by addition of 22 μ l of 10 wt% aqueous DOC solution^{41,42}. The addition of DOC prevents further reaction, and the photoluminescence spectra obtained following this step were stable for long periods (weeks)^{41,42}. Finally, another surfactant exchange into 1 wt% DOC/D₂O was performed using membrane centrifugation before measuring the ensemble photoluminescence spectra. For large-diameter (10,3) functionalization,

~50 μ l of 0.2 mg ml⁻¹ 4-methoxybenzene diazonium in D₂O was added gradually (in 10 μ l aliquots) to 200 μ l of (10,3) in 1 wt% SDS/D₂O and illuminated under E_{22} photoexcitation for 1 h. Photoexcitation was required to effectively functionalize this larger-diameter chirality^{12,43}. The reaction was quenched at the desired level of functionalization by addition of 22 μ l of 10 wt% DOC/D₂O solution.

Aryl diazonium reaction kinetics. To 160 μ l of DNA-wrapped (9,1) (0.0188 optical density in a 3 mm path length cuvette, equivalent to 0.09 μ g ml⁻¹)⁴⁴, previously exchanged into 1 wt% SDS/H₂O, were added 2 μ l of 0.05 mg ml⁻¹ aqueous solution of 4-methoxybenzene diazonium tetrafluoroborate salt. The progress of the reaction was monitored spectrofluorometrically using E_{22} illumination (700 nm), with photoluminescence spectra acquired over the course of an hour, with 30 s integration times per spectrum. Spectral monitoring was started as soon as the diazonium reagent was added to the sample cuvette, but the first intensity point was not available until the initial 30 s integration time was complete. Similarly, 2 μ l of 0.05 mg ml⁻¹ aqueous solution of 4-methoxybenzene diazonium tetrafluoroborate salt was added to 160 μ l of ATP-generated (6,5) dispersion (0.015 optical density in a 3 mm path length cuvette, also equivalent to 0.09 μ g ml⁻¹)⁴⁴, previously exchanged into 1 wt% SDS/H₂O. For (6,5) the reaction was monitored under 570 nm excitation, also for an hour. For comparison of reaction rates, we note that defect-state photoluminescence intensity I is proportional to the product of its quantum yield (QY) and the defect concentration [D]: $I \sim \text{QY}[D]$. Because QY is likely to differ for the two chiralities, a direct comparison of the change in I with time will not accurately represent any difference in reaction kinetics. To remove QY from the comparison, we normalized I at any given time to the maximum intensity (I_{max}) corresponding to the maximum obtained [D] once the reaction had run to completion. Plotting I/I_{max} versus reaction time then provides a valid comparison of reaction rates, and also a comparison of the time it takes for the reaction to reach completion in each system. Because reactions for (6,5) and (9,1) were run under identical starting concentrations of SWCNT and diazonium reagent, such a comparison is valid.

Photoluminescence spectroscopy. Solution-phase ensemble photoluminescence spectra were obtained for SWCNT samples in D₂O using a Horiba Nanolog spectrofluorometer incorporating an 850 nm long-pass filter in the collection path. Excitation was at or near the E_{22} maximum for each specific chirality: 570 nm for (6,5), 650 nm for (7,5), 635 nm for (10,3), 700 nm for (9,1) and 750 nm for (11,0). Spectral intensities were corrected for variation in excitation lamp intensity with excitation wavelength, and also for the wavelength dependence of instrument throughput and detector sensitivity. Single tube spectroscopic measurements were taken from a sample highly enriched in the (11,0) chirality, dropcast onto a glass substrate, and obtained using a home-built microscope–photoluminescence system at temperatures between 3.9 and 5 K, as described previously²². Samples were excited (at the (11,0) phonon sideband) with 2 μ W of 870 nm light from a pulsed (150 fs, 90 MHz) Ti:sapphire laser. Spectra were collected on a one-dimensional InGaAs linear array (Pylon-IR 1024-1.7, Princeton Instruments). Although the spectra of the individual nanotubes were not corrected for instrument response, the InGaAs detector array exhibited a flat response in the wavelength region of interest. Measurements of second-order photon correlation ($g^{(2)}(t)$) functions were obtained as previously described¹². Briefly, light collected from the microscope system was coupled into two channels of a superconducting nanowire single-photon detector, with photon detection events recorded using HydraHarp 400 time-correlated single-photon-counting electronics.

Theory. Functionalization was performed through the addition of both a p-aryl bromide and hydrogen at separate carbon atoms. As previously shown for (6,5)²⁵, such defects can be created in three unique *ortho* and *para* configurations defined by the bond angle with respect to the SWCNT axis (Fig. 1b). The binding stabilities of each defect configuration were determined by subtracting the total energy of the most stable conformation from the configuration of interest. Thus, the stabilities given for each binding configuration (Supplementary Fig. 4) are not enthalpies of formation per se (no information as to the initial state before a reaction is taken into account), but are simply relative stabilities. Prediction of spectral features for each configuration was accomplished by implementing DFT and linear-response TD-DFT to optimize excited-state geometries and compute energies of emission features, respectively, using the Gaussian 09 software package⁴⁵. Such methodologies rely on the use of the CAM-B3LYP density functional⁴⁶ and STO-3G basis set⁴⁷, as previously described²². A novel approach for systematically correcting the transition energies based on exciton localization was implemented^{23,48}. We note that, for SWCNT structures with $(n-m) = 7$ (such as the (10,3) chirality), tube-end capping schemes^{22,25} are problematic. Accordingly, results for (10,3) are not included so as to avoid computational artefacts. See Supplementary Information for more details on the computational methods used.

Data availability. The data that support the findings of this study are available from the corresponding authors upon reasonable request.

Received: 26 February 2018; Accepted: 25 July 2018;
Published online: 03 September 2018

References

1. Michler, P. et al. Quantum correlation among photons from a single quantum dot at room temperature. *Nature* **406**, 968–970 (2000).
2. Miyazawa, T. et al. Single-photon emission at 1.5 μm from an InAs/InP quantum dot with highly suppressed multi-photon emission probabilities. *Appl. Phys. Lett.* **109**, 132106 (2016).
3. Srivastava, A. et al. Optically active quantum dots in monolayer WSe₂. *Nat. Nanotech.* **10**, 491–496 (2015).
4. He, Y.-M. et al. Single quantum emitters in monolayer semiconductors. *Nat. Nanotech.* **10**, 497–501 (2015).
5. Koperski, M. et al. Single photon emitters in exfoliated WSe₂ structures. *Nat. Nanotech.* **10**, 503–506 (2015).
6. Chakraborty, C., Kinnischtzke, L., Goodfellow, K. M., Beams, R. & Vamivakas, A. N. Voltage-controlled quantum light from an atomically thin semiconductor. *Nat. Nanotech.* **10**, 507–512 (2015).
7. Tran, T. T., Bray, K., Ford, M. J., Toth, M. & Aharonovich, I. Quantum emission from hexagonal boron nitride monolayers. *Nat. Nanotech.* **11**, 37–41 (2016).
8. Hogege, A., Galland, C., Winger, M. & Imamoglu, A. Photon antibunching in the photoluminescence spectra of a single carbon nanotube. *Phys. Rev. Lett.* **100**, 217401 (2008).
9. Walden-Newman, W., Sarpkaya, I. & Strauf, S. Quantum light signatures and nanosecond spectral diffusion from cavity-embedded carbon nanotubes. *Nano Lett.* **12**, 1934–1941 (2012).
10. Hofmann, M. S. et al. Bright, long-lived, and coherent excitons in carbon nanotube quantum dots. *Nat. Nanotech.* **8**, 502–505 (2013).
11. Ma, X., Hartmann, N. F., Baldwin, J. K. S., Doorn, S. K. & Htoon, H. Room-temperature single-photon generation from solitary dopants of carbon nanotubes. *Nat. Nanotech.* **10**, 671–675 (2015).
12. He, X. et al. Tunable room-temperature single-photon emission at telecom wavelengths from sp^3 defects in carbon nanotubes. *Nat. Photon.* **11**, 577–582 (2017).
13. Aharonovich, I., Englund, D. & Toth, M. Solid-state single-photon emitters. *Nat. Photon.* **10**, 631–641 (2016).
14. Bachilo, S. M. et al. Structure-assigned optical spectra of single-walled carbon nanotubes. *Science* **298**, 2361–2366 (2002).
15. Zheng, M. Sorting carbon nanotubes. *Top. Curr. Chem.* **375**, 13 (2017).
16. Ghosh, S., Bachilo, S. M., Simonette, R. A., Beckingham, K. M. & Weisman, R. B. Oxygen doping modifies near-infrared band gaps in fluorescent single-walled carbon nanotubes. *Science* **330**, 1656–1659 (2010).
17. Ma, X. et al. Electronic structure and chemical nature of oxygen dopant states in carbon nanotubes. *ACS Nano* **8**, 10782–10789 (2014).
18. Kwon, H. et al. Molecularly tunable fluorescent quantum defects. *J. Am. Chem. Soc.* **138**, 6878–6885 (2016).
19. Piao, Y. M. et al. Brightening of carbon nanotube photoluminescence through the incorporation of sp^3 defects. *Nat. Chem.* **5**, 840–845 (2013).
20. Miyauchi, Y. et al. Brightening of excitons in carbon nanotubes on dimensionality modification. *Nat. Photon.* **7**, 715–719 (2013).
21. Akizuki, N., Aota, S., Mouri, S., Matsuda, K. & Miyauchi, Y. Efficient near-infrared up-conversion photoluminescence in carbon nanotubes. *Nat. Commun.* **6**, 8920 (2015).
22. He, X. et al. Low-temperature single carbon nanotube spectroscopy of sp^3 quantum defects. *ACS Nano* **11**, 10785–10796 (2017).
23. Shiraki, T., Shiraishi, T., Juhász, G. & Nakashima, N. Emergence of new redshifted carbon nanotube photoluminescence based on proximal doped-site design. *Sci. Rep.* **6**, 28393 (2016).
24. Maeda, Y. et al. Tuning of the photoluminescence and up-conversion photoluminescence properties of single-walled carbon nanotubes by chemical functionalization. *Nanoscale* **8**, 16916–16921 (2016).
25. Gifford, B. J., Kilina, S., Htoon, H., Doorn, S. K. & Tretiak, S. Exciton localization and optical emission in aryl-functionalized carbon nanotubes. *J. Phys. Chem. C* **122**, 1828–1838 (2017).
26. Strano, M. S. et al. Electronic structure control of single-walled carbon nanotube functionalization. *Science* **301**, 1519–1522 (2003).
27. Niyogi, S. et al. Chemistry of single-walled carbon nanotubes. *Acc. Chem. Res.* **35**, 1105–1113 (2002).
28. Bekyarova, E. et al. Effect of covalent chemistry on the electronic structure and properties of carbon nanotubes and graphene. *Acc. Chem. Res.* **46**, 65–76 (2013).
29. Chua, C. K. & Pumera, M. Covalent chemistry on graphene. *Chem. Soc. Rev.* **42**, 3222–3233 (2013).
30. Vora, P. M., Tu, X., Mele, E. J., Zheng, M. & Kikkawa, J. M. Chirality dependence of the K-momentum dark excitons in carbon nanotubes. *Phys. Rev. B* **81**, 155123 (2010).
31. Niyogi, S., Densmore, C. G. & Doorn, S. K. Electrolyte tuning of surfactant interfacial behavior for enhanced density-based separations of single-walled carbon nanotubes. *J. Am. Chem. Soc.* **131**, 1144–1153 (2009).
32. Duque, J. G., Densmore, C. G. & Doorn, S. K. Saturation of surfactant structure at the single-walled carbon nanotube surface. *J. Am. Chem. Soc.* **132**, 16165–16175 (2010).
33. Tummala, N. R. & Striolo, A. SDS surfactants on carbon nanotubes: aggregate morphology. *ACS Nano* **3**, 595–602 (2009).
34. Tu, X., Manohar, S., Jagota, A. & Zheng, M. DNA sequence motifs for structure-specific recognition and separation of carbon nanotubes. *Nature* **460**, 250–253 (2009).
35. Yarotski, D. et al. Scanning tunneling microscopy of DNA-wrapped carbon nanotubes. *Nano Lett.* **9**, 12–17 (2009).
36. Shiraki, T., Uchimura, S., Shiraishi, T., Onitsuka, H. & Nakashima, N. Near infrared photoluminescence modulation by defect site design using aryl isomers in locally functionalized single-walled carbon nanotubes. *Chem. Commun.* **53**, 12544–12547 (2017).
37. Subbaiyan, N. K. et al. Role of surfactants and salt in aqueous two-phase separation of carbon nanotubes towards simple chirality isolation. *ACS Nano* **8**, 1619–1628 (2014).
38. Yomogida, Y. et al. Industrial-scale separation of high-purity single-chirality single-walled carbon nanotubes for biological imaging. *Nat. Commun.* **7**, 12056 (2016).
39. Ao, G., Streit, J. K., Fagan, J. A. & Zheng, M. Differentiating left- and right-handed carbon nanotubes by DNA. *J. Am. Chem. Soc.* **138**, 16677–16685 (2016).
40. Streit, J. K., Fagan, J. A. & Zheng, M. A low energy route to DNA-wrapped carbon nanotubes via replacement of bile salt surfactants. *Anal. Chem.* **89**, 10496–10503 (2017).
41. Hartmann, N. F. et al. Photoluminescence imaging of solitary dopant sites in covalently doped single-wall carbon nanotubes. *Nanoscale* **7**, 20521–20530 (2015).
42. Hartmann, N. F. et al. Photoluminescence dynamics of aryls sp^3 defect states in single-walled carbon nanotubes. *ACS Nano* **10**, 8355–8365 (2016).
43. Powell, L. R., Piao, Y. & Wang, Y. Optical excitation of carbon nanotubes drives localized diazonium reactions. *J. Phys. Chem. Lett.* **7**, 3690–3694 (2016).
44. Sanchez, S. R., Bachilo, S. M., Kadria-Vili, Y., Lin, C. W. & Weisman, R. B. (n,m) specific absorption cross sections of single-walled carbon nanotubes measured by variance spectroscopy. *Nano Lett.* **16**, 6903–6909 (2016).
45. Frisch, M. J. et al. *Gaussian 09* (Gaussian, Inc., 2009).
46. Yanai, T., Tew, D. P. & Handy, N. C. A new hybrid exchange–correlation functional using the Coulomb-attenuating method (CAM-B3LYP). *Chem. Phys. Lett.* **393**, 51–57 (2004).
47. Hehre, W. J., Stewart, R. F. & Pople, J. A. Self-consistent molecular-orbital methods. I. Use of Gaussian expansions of Slater-type atomic orbitals. *J. Chem. Phys.* **51**, 2657–2664 (1969).
48. Gifford, B. J. et al. Correction scheme for comparison of computed and experimental optical transition energies in functionalized single-walled carbon nanotubes. *J. Phys. Chem. Lett.* **9**, 2460–2468 (2018).
49. Kilina, S., Ramirez, J. & Tretiak, S. Brightening of the lowest exciton in carbon nanotubes via chemical functionalization. *Nano Lett.* **12**, 2306–2312 (2012).

Acknowledgements

This work was conducted in part at the Center for Integrated Nanotechnologies, a US Department of Energy, Office of Science user facility, and supported in part by the Center for Nonlinear Studies and by Los Alamos National Laboratory Directed Research and Development funds. S.K. acknowledges financial support from NSF Grant CHE-1413614 for studies of functionalized carbon nanotubes. For computational resources and administrative support, the authors thank the Center for Computationally Assisted Science and Technology (CCAST) at North Dakota State University. The authors also acknowledge the LANL Institutional Computing (IC) Program for providing computational resources. H.K. acknowledges support from JSPS KAKENHI grant no. JP25220602. Correspondence and requests for materials should be addressed to S.K.D. or S.T.

Author contributions

S.K.D. conceived and designed the experiments. Nanotube separations, functionalization, and spectroscopic characterization were performed by A.S. with assistance from X.H. under the supervision of S.K.D. Single-nanotube spectroscopy was performed by X.H. under the supervision of H.H. Additional purified nanotube material was provided by G.A., M.Z. and H.K. Theoretical modelling was performed by B.J.G. under the supervision of S.T. and S.K. All authors contributed to the analysis and interpretation of results. A.S., B.J.G., S.T. and S.K.D. wrote the manuscript with assistance from all co-authors.

Competing interests

The authors declare no competing interests.

Additional information

Supplementary information is available for this paper at <https://doi.org/10.1038/s41557-018-0126-4>.

Reprints and permissions information is available at www.nature.com/reprints.

Correspondence and requests for materials should be addressed to S.T. or S.K.D.

Publisher's note: Springer Nature remains neutral with regard to jurisdictional claims in published maps and institutional affiliations.